MULTI-DIMENSIONAL GEOSPATIAL DATA INTEGRATION FOR COASTAL CHANGE ANALYSIS

R. Li [a,*], S. Deshpande[a], X. Niu[b], I-C. Lee[a], B. Wu[a]

[a]Mapping and GIS Laboratory, CEEGS, The Ohio State University 470 Hitchcock Hall, 2070 Neil Avenue, Columbus, OH 43210-1275, U.S.A-(li.282, deshpande.29, lee.3007, wu.573)@osu.edu
[b]Department of Math, Physics, Computer Science, and Geomatics Troy University, Troy, AL 36082, U.S.A-(xniu)@troy.edu

KEY WORDS: Coast, Change, Analysis, LiDAR, Orthoimage, High Resolution, Satellite, Integration

ABSTRACT:

Coastal change analysis, particularly of the variation in shorelines and blufflines, is critical for coastal disaster mitigation, environmental protection, resource management, and coastal development decision making. As data from a variety of sources has become more easily available, it is highly desirable to investigate a strategy for the integration of multi-dimensional geospatial data for coastal mapping and change analysis. This paper summarizes an investigation of techniques for integrating satellite images, aerial images, and LiDAR data for high precision coastal mapping. The integration of IKONOS and QuickBird satellite stereo image pairs with aerial images for shoreline mapping and the integration of LiDAR data and aerial orthoimages for coastal bluffline extraction are both examined. Experiments using data collected at Tampa Bay, Florida, and Lake Erie, Ohio, have shown that sub-meter measurement accuracy can be achieved through these integration strategies. Using improved mapping products based on these new techniques, bluffline erosion analysis was conducted at Lake Erie near Painesville, Ohio, and correlations between bluffline recessions and various geological and meteorological factors were examined.

1. INTRODUCTION

The coast is an area of intensive interactions between land, sea, and air. More than 80 percent of the U.S. population lives within 50 miles of the coast (Mayer et al., 2004). Coastal change analysis has been listed as one of several priority issues in coastal management in the U.S. Accurate geospatial information about coastal environments and processes, both onshore and offshore, will help coastal managers to understand the effects of complex natural and anthropogenic forces in the coastal zone and to facilitate their decision-making processes for controlling coastal erosion, for example. Recent advances in geospatial technologies such as remote sensing, global positioning, data handling along with new computing technologies have dramatically changed the density, accuracy, timeliness, and inherent nature of coastal mapping data and related data products. Huge amounts of coastal information have been gathered by public agencies, academic institutions, and private companies. Advanced methods for integrating and applying these multi-source data, along with their associated levels of accuracy, could significantly improve coastal management, especially erosion control.

This paper will describe accurate coastal mapping techniques that have been developed using the integration of multi-dimensional geospatial data including satellite imagery, aerial imagery, and LiDAR data to produce such coastal mapping products as shorelines and blufflines with sub-meter level of accuracy. The resulting sub-meter level mapping products were used to analyze the influence different geological and meteorological factors on coastal changes.

2. INTEGRATION STRATEGIES FOR ACCURATE COASTAL MAPPING

2.1 Integration of satellite and aerial images for shoreline extraction

For our study, in the southern region of Tampa Bay, Florida, 24 aerial images, a pair of IKONOS and QuickBird stereo images are available that cover the same local area (Figure 1 and Table 1). It is of great importance to study the geopositioning accuracy attainable by different combinations of imagery from different sources. This section first investigates the integration of IKONOS, QuickBird, and aerial images using the data collected at Tampa Bay. Based on the results of this analysis, shoreline extraction was performed using these IKONOS and QuickBird satellite images and was compared with the water-level data from the closest gauge station.

Figure 1 shows the IKONOS and QuickBird stereo pairs and aerial images that cover the research test area. Eleven GPS ground control points were used in the present study for the aerial images. Block bundle adjustment was performed using GPS control points, five of which were used as ground control points (GCPs) and the remaining six points as check points (CKPs). These are illustrated as triangles (GCPs) and circles (CKPs) in Figure 1. Rational polynomial coefficients (RPCs) for the aerial images were acquired using virtual control points (VCPs) (Di et al., 2003), which were generated using the interior and exterior orientation parameters along with the image plane coordinates of the aerial images by assuming a suitable value for the Z-coordinates in the object space. For the satellite images, the vendor-provided RPCs are usually computed without using GCPs, which results in lower accuracy of the ground coordinates. Hence, an affine transformation was

* Corresponding author.

employed to refine the image coordinates of the satellite images as follows.

$$i' = a_0 + a_1 i + a_2 j$$
$$j' = b_0 + b_1 i + b_2 j \quad (1)$$

where, (i, j) and (i', j') represent the measured and calculated image coordinates of the GCPs, respectively. Affine transformation parameters were represented by a_0 to a_2 and b_0 to b_2. Then, the measured image coordinates of CKPs were refined using the computed affine transformation parameters. Correction was not applied to image coordinates of CKPs from aerial images as RPCs for the aerial images were obtained using VCPs thus considered more accurate. Finally, the aerial image coordinates and refined satellite image coordinates of the CKPs were used to calculate the ground coordinates of CKPs using the RPCs. The performance of various image integration schemes was then evaluated by comparing the computed ground coordinates of the CKPs with those obtained from aerial triangulation.

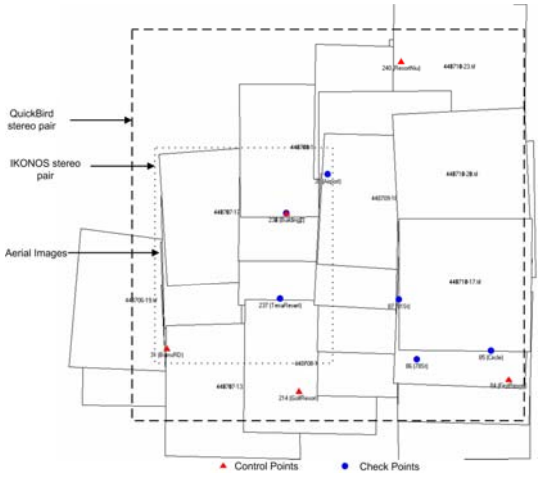

Figure 1. Distribution of GCPs and CKPs on IKONOS, QuickBird, and aerial images

Two types of combinations of satellite images and aerial images were examined. In the first type, Two pairs of IKONOS and QuickBird stereo images and 24 aerial images were considered to form seven various image networks and to study the effect of geopositioning by integrating different sets of images. Four evenly distributed GPS control points were used as GCPs, and 27 points determined by aerial triangulation were used as CKPs, which were present in the common area of the satellite and the aerial images. The 3-D geopositioning accuracies for each combination were calculated (Table 2). In the second type, the same two pairs of IKONOS and QuickBird images were integrated with only one aerial image or one pair of aerial images. The same four GPS control points were used as GCPs, and ten CKPs in the common area of the aerial stereo image pair and the satellite images were used for accuracy assessment. The results are listed in Table 3.

	QuickBird	
	Forward	**Backward**
Acquisition date	2003-09-12	2003-09-12
Acquisition time (GMT)	15:58:08	15:59:17
Image resolution	0.767 m	0.751 m
Image size (row x column)	25776 × 27552	24620 × 27552
Collection azimuth (θ)	17.7°	184.5°
Collection elevation (α)	58.7 °	59.2°
	IKONOS	
Acquisition date	2004-07-08	2004-07-08
Acquisition time (GMT)	16:17:17	16:18:08
Image resolution	1 m	1 m
Image size (row x column)	8484 × 12160	8484 × 12160
Collection azimuth (θ)	40.8°	120.1°
Collection elevation (α)	60.8°	74.1°

Table 1. Parameters of satellite stereo images

Combinations	**3-D Geopositioning Accuracy (RMSE: m)**		
	σ_x	σ_y	σ_z
IK (S)	0.770	1.241	1.058
QB (S)	0.919	0.538	0.753
IK (S) + QB (S)	0.825	0.674	0.611
AI + IK (S)	0.132	0.172	0.385
AI + QB (S)	0.248	0.125	0.346
AI + IK (S) + QB (S)	0.272	0.191	0.359
AI	0.108	0.100	0.330

Note: S: stereo; QB: QuickBird; IK: IKONOS; AI: Aerial images

Table 2. Geopositioning accuracy of the integration of satellite images and all 24 aerial images

Based on the results shown in Table 2, it was observed that the accuracy obtained by the QuikBird stereo pair is overall better than that obtained by the IKONOS stereo pair. Furthermore, accuracy obtained by the integration of the two satellite stereo pairs with the aerial images is better than that obtained by the satellite stereo pairs individually, but is not better than the accuracy obtained by the aerial images only. This demonstrates that the image network of the aerial images is strong enough. By adding the weaker (resolution and small convergence angle) components of satellite images, the geopositioning accuracy cannot be improved. On the other hand, as shown in Table 3, it was found that by adding one aerial image to the satellite image network, the accuracy obtained in the X and Y directions is better than that obtained from the satellite images alone. In addition, by adding a stereo pair of aerial images (in the along track or Y direction) to the satellite image network, the accuracy obtained is further increased in the Y direction significantly, as well as in the Z direction.

Geopositioning accuracy, particularly in elevation, using a stereo pair can be significantly affected by its formed convergence angle (Li et al., 2007; Niu et al., 2005). In this study, weak geometry is often formed by a pair of backward (or forward) -looking satellite images from the two orbits. This is demonstrated in Table 3 in the rows of "IK (B) – QB (B)" and "IK (S)" where the convergence angles are 27 degrees and 30 degrees, respectively.

Combinations	3-D accuracy after addition of one aerial image (RMSE: m)			3-D accuracy after addition of one pair of stereo aerial image (RMSE: m)		
	σ_x	σ_y	σ_z	σ_x	σ_y	σ_z
QB (S) – IK (S)	0.952	0.915	0.797	0.952	0.915	0.797
IK (B) – QB (B)	0.692	0.819	1.588	0.645	0.192	1.032
IK (F) – QB (F)	0.382	0.364	0.537	0.356	0.265	0.517
IK (S)	0.327	0.763	1.014	0.341	0.423	0.708
QB (S)	0.532	0.425	0.800	0.528	0.259	0.748
IK (B) - QB (F)	0.491	0.443	0.782	0.476	0.276	0.724
IK (F) - QB (B)	0.450	0.622	0.885	0.478	0.348	0.761

Note: S: stereo; F: forward; B: backward; QB: QuickBird; IK: IKONOS

Table 3. Geopositioning accuracy of the integration of satellite images with one or one pair of aerial images

Based on the above analysis of image integration strategies, 3-D shorelines were derived from IKONOS stereo images and QuickBird stereo images. Points along the shoreline on the satellite image pairs were manually identified, and their corresponding 3-D coordinates were calculated based on the RPCs and the refined measured image coordinates. The elevations of the derived shorelines were compared to gauge stations' water level observations. As only predicted water level at the imaging time of IKONOS images was available at the closest gauge station, real observations from two other nearest gauge stations were also used in this comparison to ensure the quality of the comparison. It was found that the QuickBird shoreline was on average 0.2 m lower and the IKONOS shoreline was on average 0.5 m higher. Both resulting differences are within the vertical accuracies of the QuickBird and IKONOS stereo images.

2.2 Integration of LiDAR data and aerial orthoimages for bluffline extraction

In addition to satellite imagery and aerial photographs, LiDAR data has been widely used recently for coastal resource management. Despite its high vertical accuracy (centimetre level), its lower horizontal accuracy limits its usefulness for mapping shorelines, which requires highly accurate position information. To improve the accuracy of shoreline mapping, a new method for coastal bluffline extraction has been developed using the integration of LiDAR data with high-resolution orthoimages.

This study looked at an area located in Painesville, Ohio along the southern shore of Lake Erie (Figure 3a) that has been identified as highly vulnerable to severe erosion (Zuzek et al., 2003; Srivastava et al., 2005). Two bluff regions, Region 1 and Region 2 (extending 670 m and 2 km, respectively) were used in this research for bluffline extraction (Figure 3a). The LiDAR data was collected in December, 1998 using a LiDAR sensor of the ATM (Airborne Topographic Mapper). Accuracy was 15 cm and 0.8 m in the vertical and horizontal directions, respectively. The nominal ground spacing was 3 m. The aerial orthoimages were collected in April, 2000. The ground resolution of the orthoimages was 0.15 m. In this area, historical blufflines are also available.

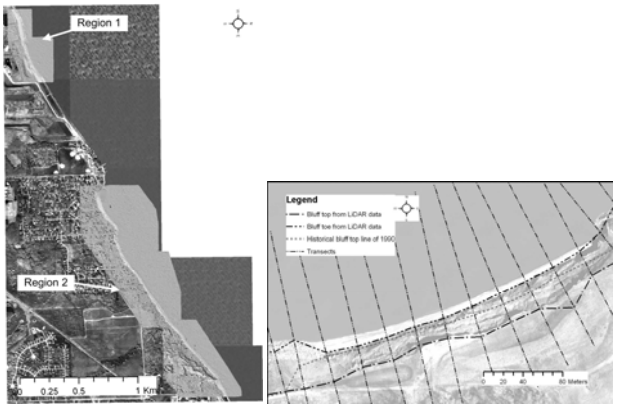

(a) (b)

Figure 3. (a) Orthoimages showing the shaded study regions along the Ohio shoreline of Lake Erie and (b) orthoimage for Region 1 showing the initial blufflines extracted from LiDAR data, historical bluff top line, and transects perpendicular to the historical bluff top line

In this research, a bluffline from start point A_1 to end point A_{n+1} (represented as A_1A_{n+1}) was divided into a finite number (n) of segments A_1A_2, A_2A_3, ..., A_nA_{n+1} that were defined by their start and end points A_1 (x_1, y_1, z_1), A_2 (x_2, y_2, z_2), ..., A_n (x_n, y_n, z_n), and A_{n+1}(x_{n+1}, y_{n+1}, z_{n+1}). These segments of sufficiently short distances can be approximated as bluffline. The blufflines thus extracted from the images and LiDAR data will be a sequence of detected bluff top or toe points separated by short distance.

It was found that in the 3.2 km length of shoreline examined in this experiment the bluff height ranged from 6 m to 24.3 m. Spikes exist in the raw LiDAR data. Median filter was used to filter the noises and to minimize the spikes. After filtering, the orthoimages were superimposed on the filtered data and a comparison was made to ensure that topographic features were not removed. A historical bluffline (bluff top) was used as a reference line to create a series of perpendicular transects (Figure 3b). The average distance between the transects was 30 m. Three-dimensional elevation profiles were then generated along transects from the LiDAR digital surface model (DSM) and the bluff top and bluff toe were defined as shown in Figure 4a. The bluff top and toe was determined by analyzing the elevation information from the LiDAR data set along the profile using the following unique characteristics: the variation of the slope along the elevation profile is generally greater at these two positions than anywhere else. The elevation profiles consisted of a sequence of linearly interpolated points from the LiDAR data with a uniform spacing *d*. Backward slope at Point *i* (*i* = 1, 2, …, *n*, increasing from water toward land) at *m* different scales based on a backward difference was computed as:

$$BSlope_i^{\,j} = \frac{H_{i+1} - H_{i-j+1}}{j \cdot d} \tag{2}$$

where, H_i is the elevation at Point *i*, *j* is the point index interval from Point *i* toward the water, and *j* = 1, 2, 3, …, *m*. For example, when *j* = 1, $BSlope_i^1 = H_{i+1} - H_i / d$ and when *j* = 2, $BSlope_i^2 = H_{i+1} - H_{i-1} /(2 \cdot d)$.

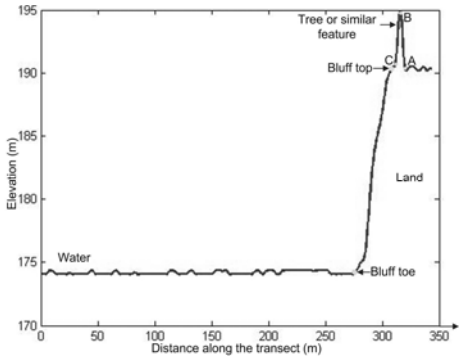

(a)

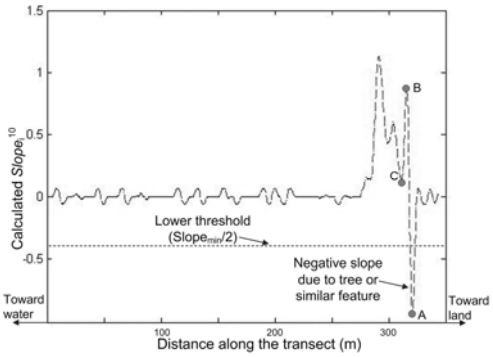

(b)

Figure 4. Elevation profile along a transect and slope variation: (a) typical 3-D elevation profile along a transect and influence caused by objects near the bluff top, and (b) slope profile

It should be noted that sometimes vertical structures (such as trees) can be found near the bluff top that create a large change in slope yet do not represent the bluff top. Therefore, these vertical features need to be identified and excluded. For the elimination of such vertical features from the slope profile, it was assumed that these vertical features were symmetrical about their peak points based on the observation that in the slope profile such a vertical feature shows a large slope increase and also a more significant slope decrease due to symmetry. By scanning the slope profile (Figure 4b) from land to water, a point with a local minimum slope was identified. Theoretically, the central slope of the peak point B should be equal to zero. Based on the definition of slope, however, Point B was the next peak point adjacent to Point A. Because of the assumption of symmetry of the vertical feature, the horizontal distance between Points B and A along the transect should be equal to half of the bottom width of the feature. Once Points A and B are identified, Point C that was symmetric about Point B was identified. In practice, there could be multiple vertical features on the top of the bluff. These features were detected from the slope profile by examining the slope values. Considering the elevation profile spacing where d = 0.5 m, a $BSlope_i^{10}$ a value of -0.4 can be obtained from a feature two meters above a relatively flat ground. For this research site, features taller than this height were identified by the following criterion. If the minimum slope along the elevation profile ($BSlope_{\min}$) was lower than -0.4, all the points below the threshold $BSlope_{\min}/2$ were considered to be vertical feature candidates. The vertical features thus identified were excluded in the process of bluff top determination.

After the backward slopes at the points along the transect have been calculated using Equation 2, a slope constraint (SC) was then defined as SC = $BSlope_{max}/4$. The bluff top candidates along the slope profile were determined as those points that had slope value $BSlope_i^{10} \geq SC$. Since there was no significant slope increase beyond the bluff top point, the numbers of the candidates identified above were then reduced by checking each point to satisfy the criteria $BSlope_i^{10} \geq BSlope_{i+1}^{10}$. The above two steps identified multiple bluff top candidates. The point with maximum elevation was identified as the bluff top. A similar procedure was adopted on an inverted profile of the transects to obtain the bluff toe point. The algorithm described above was repeated for all elevation profiles. The identified 3-D bluff top and toe points were then connected across the profiles to form the initial blufflines (top and toe).

	Digitized bluffline vs. LiDAR bluffline (m)			**Digitized bluffline vs. refined bluffline (m)**		
	X	**Y**	**Z**	**X**	**Y**	**Z**
Region 1: bluff top	1.41	3.90	0.51	0.63	1.23	0.17
Region 2: bluff top	1.08	2.20	0.88	0.52	0.89	0.40
Combine: bluff top	1.18	2.69	0.77	0.55	0.99	0.34
Region 1: bluff toe	0.54	1.72	0.38	0.19	0.51	0.07
Region 2: bluff toe	1.13	2.35	0.65	0.39	0.86	0.21
Combined bluff toe	0.96	2.17	0.57	0.33	0.76	0.17

Table 4. Comparison of blufflines derived from different sources.

The initial blufflines derived from LiDAR data were superimposed on the orthoimage. In most locations these initial blufflines were very close to the corresponding features seen on the orthoimage. However, at some positions the lines deviate significantly from the orthoimage positions. Therefore, the initial blufflines were refined through the following steps. First, mean-shift segmentation (Comaniciu and Meer, 2002) followed by a surface reconstruction method (Kovesi, 2003) was applied to the orthoimages to enhance image edge features. Second, an edge detection technique was used to extract the blufflines from the surface-reconstructed image. Third, Iterative Closest Point (ICP) algorithm (Besl and McKay, 1992; Nikolaidis and Pitas, 2001) was applied to refine the planimetric positions of the blufflines extracted from the LiDAR data using the edges detected from the orthoimages. Finally, the Z-coordinates of the refined blufflines were interpolated from LiDAR data at the refined point positions.

Both blufflines extracted from LiDAR data and the blufflines resulting from refinement using orthoimages were compared with blufflines manually digitized from the orthoimages. Averages of the absolute differences between the two lines in 3-D coordinates (X: east; Y: north; and Z: elevation) were calculated at points where the transects intersect the corresponding blufflines. The results, summarized in Table 4, show that, the refined blufflines using orthoimages are better horizontally than the blufflines directly extracted from LiDAR data, the refined bluff top and bluff toe lines are closer to the manually digitized blufflines.

3. COASTAL EROSION ANALYSIS

To further understand the mechanism of coastal erosion and to facilitate the analysis of factors that cause changes along the coast, coastal change information was derived based on the above accurate coastal mapping products and historical coastal geospatial information. To study this technique, coastal change analysis was conducted along the southern coast of Lake Erie in the Painesville area in Ohio. In this area, coastal erosion has been a major cause of significant loss of property over the past decades, with an annual erosion rate above 1.03 m per year over the period from 1973 to 2000. The data collected and used in this research includes measured blufflines, elevation and slopes of blufflines, wind speed and direction, wave height and direction, water level, storm events, precipitation, soil type, and land use.

The blufflines were measured in 1973, 1990, 1994, 2000, and 2004 from the integration of multi-source data. Wind and wave information for the period 1973 to 1987 were acquired from the WISWAVE model created by the NOAA Great Lakes Environmental Research Laboratory (GLERL). Wind and wave data for the period 1988-2004 were acquired from Lake Erie Buoy No. 45005 (near Cleveland), which is approximately 60 miles from Painesville. Data on water levels was extracted from the Cleveland gauge station managed by the NOAA Center for Operational Oceanographic Products and Services (CO-OPS). This gauge station is approximately 30 miles from Painesville. Data on storm events for the area near Painesville for the period 1973-2004 was gathered from the NOAA National Climatic Data Center (NCDC). Data on precipitation for the period 1973-2004 was acquired for the Painesville area from the NOAA National Weather Service. Two different sources for land cover and land use data were used: the Ohio Department of Natural Resources (ODNR), and the NOAA Coastal Service Center (CSC). Elevation and slope data for the bluffline were gathered from the collected digital elevation models (DEMs). The only DEMs available at the time of this analysis were for 2000 and 2004.

In our analysis, recession rate was used to estimate bluffline erosion. The recession rate at Lake Erie in the Painesville area was calculated based on recession distances measured between blufflines from five different years: 1973, 1990, 1994, 2000, and 2004. A reference line connecting the extreme end points of the 1973 bluffline was formed and perpendicular transects linking each point on the bluffline were produced. The transects were extended to intersect other blufflines. Each point where the transect lines intersected other bluffline polylines were selected as a new node. The distance along the transect line between different blufflines was then calculated using the new nodes and the points on the 1973 bluffline. This difference was the recession distance for each measured point over the period between the two blufflines. Recession rates were calculated based on the calculated recession distances and the number of years relevant to each individual analysis. The analysis was performed at both regional and local scales as follows (Li et al., 2008).

3.1 Analysis at the regional scale

The goal of analysis of erosion factors at the regional scale was to find out which factor(s) were linked directly to the recession rate. Five factors (wind speed, wave height, precipitation, water level, and storm events) were employed in this regional analysis. These factors were related to shoreline change (Hanson and Kraus, 1989) and thus could also be factors in bluffline change.

Relationships between factor pairs were first analyzed before considering recession rate. It was found that annual mean wind speed and annual mean wave height were highly correlated. Similarly, it was found that there was a positive correlation between precipitation and wind speed (0.45 correlation coefficient). The relationship between precipitation and wave height also showed a positive correlation between the two factors (0.47 correlation coefficient). Other factors did not show significant correlation.

Comparisons of recession rate to wind speed, wave height, regular daily wind speed, and wave action did show correlation. A strong correlation (0.94) between recession and wind speed in storm events was found. Similarly, a strong correlation (0.9) was found between recession rate and average hourly water level

3.2 Analysis at the local scale

In the local analysis, the influence on recession rate of factors such as: bluff top elevation, slope of the bluff top, curvature of the bluffline, and the soil type and land use type of the bluff top were analyzed. It was observed that average recession is larger wherever elevation was lower and smaller wherever elevation was higher. Further, it was found that higher slope at the bluff top would produce a higher recession rate. Curvature was calculated using three consecutive nodes along the bluffline. Positive curvature represents a bay, and negative curvature represents the location where the land stretches into the water. It was found that larger the curvature, the larger the recession, making negative curvature an important factor in bluffline erosion.

In the comparison between land use and land cover (LULC) along with soil type and recession rate, it was found that Swanton fine sandy loam and Painesville fine sandy loam soil types had more erosion than other soil types in the region under similar LULC conditions. It was also found that significant erosion happened in urban areas where the soil type was Swanton fine sand loam. In was noted that among all the soil types represented in the test area, the two soil types with the largest recession have the smallest K factors (soil erodibility factor), which may relate to the erosion pattern in this region.

4. CONCLUSIONS

This paper represents methods to integrate geospatial data sets from multiple sensors to increase mapping accuracy and their application to coastal management and coastal change analysis. Based on the analysis and experiments, it can be concluded that:

1) Geopositioning accuracy of satellite images can be enhanced by adding higher resolution aerial images (even just a stereo pair). However, it was found that the improved accuracy would not be better than that of aerial images that form a strong network. Further, the extracted shorelines from the integrated satellite images have a vertical accuracy of ±0.2 m to 0.5 m compared to the gauge station data, which is within the elevation uncertainty of the satellite images.
2) The blufflines derived from the integration of airborne LiDAR data and orthoimages are closer to the manually

digitized blufflines and demonstrated that such an integration enhanced the overall shoreline quality compared to those extracted from either one of the data sources.

3) In the analysis of bluffline recession in the Painesville area, it was found that water level and wind speed in storm events are the major factors associated with bluffline recession. Other factors that affected bluffline recession were elevation and slope of the bluff and curvature of the bluffline. It was also found that significant erosion happens in urban areas where the soil type is Swanton fine sand loam.

REFERENCES

Besl, P., and N. McKay, 1992. A method of registration of 3-D shapes, *IEEE Transactions on Pattern Analysis and Machine Intelligence,* 14(2), pp. 239-256.

Comaniciu, D., and P. Meer, 2002. Mean shift: a robust approach toward features space analysis, *IEEE Transactions on Pattern Analysis and Machine Intelligence*, 24(5), pp. 603-619.

Di, K., R. Ma, and R. Li, 2003. Rational functions and potential for rigorous sensor model recovery. *PE&RS*, 69(1), pp. 33-41.

FGCD (Federal Geographic Data Committee), 1998. Geospatial Positioning Accuracy Standards Part 3: National Standard for Spatial Data Accuracy. http://www.fgdc.gov/standards/projects/FGDC-standards-projects/accuracy/part3/chapter3. (last date accessed: 14 September, 2007)

Hanson, H., and N.C. Kraus, 1989. GENESIS: Generalized model for simulating shoreline change. Tech. Rep. CER-89-19, USAE-WES.

Kovesi, P.D., 2003. Shapelets correlated with surface normals produce surfaces. Technical report. URL http://www.csse.uwa.edu.au/pk/, School of computer science and software engineering, the University of Western Australia (last date accessed: 9 October, 2003).

Li, R., F. Zhou, X. Niu, and K. Di, 2007. Integration of IKONOS and QuickBird imagery for geopositioning accuracy analysis. *PE&RS*, 73(9), pp. 1067-1074.

Li, R., K. Bedford, X. Niu, B. Wu, S. Deshpande, I-C. Lee, V. Velissariou, and F. Zhou, 2008. Seamless Integration from Water to Land. NGA Final Report, The Ohio State University.

Mayer, L.A., K.E. Barbor, P.R. Boudreau, T.S. Chance, C.H. Fletcher, H. Greening, R. Li, C. Mason, S. Snow-Cotter, D.J. Wright, R.S. Lewis, D.A. Feary, T. Schaefer, Y. Forsbergh, B. Mason, and A. Schrum, 2004. A Geospatial Framework for the Coastal Zone: National Needs for Coastal Mapping and Charting, The National Academies Press, Washington, D.C., 149 p.

Nikolaidis, N., and I. Pitas, 2001. 3-D Image Processing Algorithms. John Wiley and Sons, 176 p.

Niu, X., F. Zhou, K. Di, and R. Li, 2005. 3D Geopositioning accuracy analysis based on integration of QuickBird and IKONOS imagery. *Proceedings of the ISPRS Workshop "High Resolution Earth Imaging for Geospatial Information"*, Hannover, Germany, May 17-20, 2005.

Shalowitz, A. L., 1964. Shore and Sea Boundaries. U.S. Department of Commerce, National Oceanic and Atmospheric Administration, National Ocean Service. 631p.

Srivastava, A., X. Niu, K. Di, and R. Li, 2005. Shoreline modelling and erosion prediction, *Proceedings of ASPRS Annual Conference, Baltimore*, unpaginated CD-ROM.

Zuzek, P.J., B.N. Robert, and J.T. Scott, 2003. Spatial and temporal considerations for calculating shoreline change rates in the Great Lakes basin, *Journal of Coastal Research,* 38: pp. 125-146.

ACKNOWLEDGEMENTS

This research is supported by the National Science Foundation CEO-P program and the National Geospatial-Intelligence Agency.